A Temporal Phase Coherence Estimation Algorithm and Its Application on DInSAR Pixel Selection

Feng Zhao, *Student Member, IEEE*, and Jordi J. Mallorqui, *Senior Member, IEEE*

***Abstract*—Pixel selection is a crucial step of all advanced DInSAR techniques that has a direct impact in the quality of the final DInSAR products. In this paper a full-resolution phase quality estimator, i.e. the temporal phase coherence (TPC), is proposed for DInSAR pixel selection. The method is able to work with both distributed (DS) and permanent (PS) scatterers. The influence of different neighboring window sizes and types of interferograms combinations (both the single-master and the multi-master) on TPC has been studied. The relationship between TPC and phase standard deviation of the selected pixels has also been derived. Together with the classical coherence and amplitude dispersion methods, the TPC pixel selection algorithm has been tested on 37 VV polarization Radarsat-2 images of Barcelona Airport. Results show the feasibility and effectiveness of TPC pixel selection algorithm. Besides obvious improvements on the number of selected pixels, the new method shows some other advantages comparing with the other classical two. The proposed pixel selection algorithm, which presents an affordable computational cost, is easy to be implemented and incorporated into any advanced DInSAR processing chain for high quality pixels' identification.**

***Index Terms*—Differential synthetic aperture radar (SAR) interferometry (DInSAR), pixel selection, temporal phase coherence (TPC), classical spatial coherence (SPC), amplitude dispersion (D_A).**

I. Introduction

DIFFERENTIAL interferometric synthetic aperture radar (DInSAR), as a remote sensing technique, can provide high resolution ground deformation monitoring results efficiently [1], [2]. Theoretically, the precision of DInSAR measurements can reach up to millimeter level [3], which makes it a powerful tool in land motion detection. Interferometric phase, which directly determines the precision of the final DInSAR products, is the most crucial element in the whole processing chain. However, due to the influence of the different decorrelation sources, mainly temporal, geometrical and volumetric [4], the phase quality is undermined. To guarantee the quality of the derived results, only those pixels that preserve their phase quality along time can be used for information exploitation in advanced DInSAR techniques. Therefore, an adequate pixel selection able to identify these high quality pixels is essential and mandatory before the application of any advanced DInSAR technique.

Two classical criterions, the amplitude dispersion (D_A) [5] and the coherence stability (γ) [6]–[8], have been widely utilized to complete the pixel selection. D_A allows to detect those pixels dominated by the so-called deterministic or permanent scatterers (PS) that are time-invariant and spatially concentrated. Typically, with enough images the D_A can be taken as an accurate approximation of the phase standard deviation (STD) [5]. So pixels with a D_A lower than a given threshold can be chosen as PS pixels. On the one hand, this pixel selection criterion works at pixel level and thus can preserve the resolution of the Single Look Complex (SLC) image. On the other hand, it works for point-like scatterers affected by low speckle noise. When it is applied into natural environments, where distributed scatterers (DS) account for the majority, few pixel will be selected. Moreover, a large number of SAR images, usually more than 20 [5], are required to assure the reliability of the method.

As the interferometric coherence is a measure of the phase quality [9], [10], it can be used as a pixel selection criterion. The coherence is estimated over multi-looked interferograms, so it implies a reduction on the resolution. Similarly to the previous method, a threshold can be set to select pixels above an established phase quality, i.e. those with coherence values higher than the threshold. On the one hand, this criterion is suitable for a more extended range of scenarios, since it can work with Distributed Scatterers (DS) but can also detect PSs. The reduction in resolution can be compensated by the fact that even a small amount of SAR images can provide a reliable result.

To overcome the shortcomings of the two classical pixel selection methods, more advanced algorithms have been investigated [11]–[17]. Most of these algorithms require to carry out a similarity estimation before the calculation of phase quality estimator, which is very time consuming especially for large SAR data sets and large study areas.

In this paper, we present a phase quality assessment and pixel selection approach for advanced DInSAR processing. The proposed algorithm is similar to the conventional coherence method, but it estimates the phase coherence temporally. Since the conventional coherence is estimated based on the spatial neighboring pixels and the new coherence is obtained in the temporal dimension, we refer the classical coherence as spatial coherence (SPC) and the new coherence as temporal phase coherence (TPC), hereafter. As the coherence is now evaluated temporally at pixel level, the method is able to work on both PS and DS pixels. The idea of TPC is similar with

Manuscript received **** **, ****; revised **** **, ****. This work was supported by China Scholarship Council (CSC NO. 201606420041), by the Spanish Ministry of Economy, Industry and Competitiveness (MINECO), the State ResearchAgency (AEI) and the European Funds for Regional Development (EFRD) under project TEC2017-85244-C2-2-P, and by the National Natural Science Foundation of China (Grant 51574221, 41874044). CommSensLab is Unidad de Excelencia Maria de Maeztu MDM-2016-0600 financed by the Agencia Estatal de Investigacin, Spain.

Feng Zhao and J. J. Mallorqui are with the CommSensLab, Universitat Politècnica de Catalunya, 08034 Barcelona, Spain (e-mail: feng.zhao@tsc.upc.edu; mallorqui@tsc.upc.edu).

that was proposed by Hooper [18], but we use a different way to estimate it. Also, the influence of different interferograms' combinations on the estimation of TPC and its relationship with the interferometric phase standard deviation (phase STD), which have not been sufficiently discussed in Hooper's paper [18], [19], have been deeply investigated.

This paper is organized as follows. Section II presents the basic concept of SPC and the algorithm for TPC estimation. In addition, the influence of different types of interferogram combinations on TPC and the relationship between TPC and phase standard deviation (STD) are studied. In Section III, the test site and data set, which are used to evaluate the feasibility of TPC, are briefly described. Then, the pixel selection and ground deformation monitoring results based on TPC and the other two classical methods are compared in Section IV. After that, in Section V and VI some discussions are made. Finally, conclusions are given in VII.

II. Methodology

A. Spatial Coherence (SPC) Estimation

The spatial coherence γ_{SPC} of one pixel in an interferogram can be expressed as [2]

$$\gamma_{SPC} = \mid \gamma_{SPC} \mid \cdot e^{j\psi} = \frac{E[S_1 \cdot S_2^*]}{\sqrt{E[\mid S_1 \mid^2] \cdot E[\mid S_2 \mid^2]}} \quad (1)$$

where S_1 and S_2 are the complex pixels of the two SAR images forming the interferogram, $E[]$ and $*$ stand for the expectation and conjugate operator, respectively. The modulus $\mid \gamma_{SPC} \mid$ of the complex coherence, which varies between the range [0, 1], indicates the quality of the interferometric phase ψ. With 1 for fully correlated data, and 0 for totally uncorrelated data. Ideally, a large number of interferograms, which should be acquired under identical circumstances, would be needed to obtain the expectation values in (1). However, this is impossible as every pixel is observed only once during each SAR acquisition [20].

In practical situations, the accuracy of phase observations of a uniform region is assumed to be stationary. Under the assumption of ergodicity, the expectation operator in (1) is replaced by the spatial average, leading to the maximum likelihood estimator $\mid \hat{\gamma}_{SPC} \mid$

$$\mid \hat{\gamma}_{SPC} \mid = \frac{\mid \Sigma_{n=1}^{N} S_1^n \cdot (S_2^n)^* \mid}{\sqrt{\Sigma_{n=1}^{N} \mid S_1^n \mid^2 \cdot \Sigma_{n=1}^{N} \mid S_2^n \mid^2}} \quad (2)$$

where N indicates the number of looks, i.e. the effective number of independent pixels involved in the spatial averaging [20]. For simplicity, $\hat{\gamma}_{SPC}$ means the value of $\mid \hat{\gamma}_{SPC} \mid$ hereafter. We will also distinguish along the paper between the true value of the coherence, γ_{SPC} which is unknown when working with real data, and the estimated one, $\hat{\gamma}_{SPC}$.

B. Temporal Phase Coherence (TPC) Estimation

After removing the topographic term by using an external DEM, the phase of a differential interferogram can be expressed for each pixel as (3)

$$\psi = \psi_{def} + \psi_{atm} + \psi_{orb} + \psi_{\xi_{DEM}} + \psi_{noise} \quad (3)$$

where ψ_{def}, ψ_{atm} and ψ_{orb} denote the phase terms introduced by the deformation along the line of sight (LOS) direction, atmospheric artifacts and SAR satellite orbit indeterminations. $\psi_{\xi_{DEM}}$ is the residual phase due to the DEM errors, and ψ_{noise} is the noise phase term, which can be associated to all decorrelation processes affecting the pixel. This latter term would present a random behaviour with respect other pixels, while the other terms can be assumed to be deterministic and, in principle, correlated with the neighboring ones. This spatial low-pass behavior can be clearly applied to the atmospheric artifacts and the orbital errors while for the deformation and the DEM error terms could be an acceptable approximation. The noise phase term can be used as a metric of pixel's phase quality and so to identify those pixels with good phase quality along time. These pixels are named Persistent Pixels (PPs). This model can be applied to both PS and DS pixels as the method would estimate ψ_{noise} for a given pixel, but the physical source of its noise plays no role.

The Temporal Phase Coherence (TPC) can be used to evaluate the quality of a pixel from the behavior of its phase noise along the interferometric stack,

$$\hat{\gamma}_{TPC} = \frac{1}{M} \cdot \mid \sum_{i=1}^{M} e^{j \cdot \psi_{noise,i}} \mid \quad (4)$$

where M is the number of interferograms and $\psi_{noise,i}$ is the noise phase term of the ith interferogram. For a given pixel, the noise term for each interferogram is estimated after minimizing the deterministic terms using its neighboring pixels.

Before introducing the details of the TPC method some basic concepts are given first.

1) Central and neighboring pixels

The *central pixel* is the pixel whose phase noise is being estimated, and the *neighboring pixels* are those pixels surrounding the central one within the extend of an estimation window, as Fig. 1 shows.

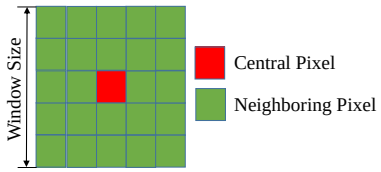

Fig. 1. Central and neighboring pixels within the estimation window.

2) TPC estimation

The detailed steps of TPC estimation are presented as follows:

a) Neighboring pixels' mean phase calculation: The mean phase of the neighboring pixels is determined by averaging their complex values and then calculating the argument of the average,

$$\widetilde{\psi}^{neigh} = \arg\langle \sum_{i=1}^{N} A(i) \cdot e^{j \cdot \psi(i)} \rangle \quad (5)$$

where $A(i)$ is the pixel's amplitude and N the number of neighboring pixels included in the estimation window. The

number of neighbouring pixels averaged depends on the extension of the estimation window (for instance 21×21, but excluding the central pixel). Similarly to the classical multi-looking in interferometry, the pixels' amplitudes are used in order to give more significance to those pixels with higher amplitudes in front of those with lower ones that, in principle, can be expected to be noisier and less reliable.

b) Spatial low-pass components cancelation: The phase of the central pixel follows the model presented in (3),

$$\psi^{central} = \psi^{central}_{def} + \psi^{central}_{atm} + \psi^{central}_{orb} + \psi^{central}_{\xi_{DEM}} + \psi^{central}_{noise}. \quad (6)$$

Similarly, the mean phase of the neighbouring pixels can be also decomposed in the same terms,

$$\widetilde{\psi}^{neigh} = \widetilde{\psi}^{neigh}_{def} + \widetilde{\psi}^{neigh}_{atm} + \widetilde{\psi}^{neigh}_{orb} + \widetilde{\psi}^{neigh}_{\xi_{DEM}} + \widetilde{\psi}^{neigh}_{noise}. \quad (7)$$

If this phase is subtracted, in the complex domain, to the phase of the central pixel,

$$\psi^{dif} \equiv \psi^{central} - \widetilde{\psi}^{neigh} \quad (8)$$

a differential phase is obtained. Clearly the atmospheric artifacts and orbital phase terms present a spatial low-pass behavior. Thus, these terms of the central pixel, (6), and the ones of the mean phase of the neighboring pixels, (7), can be considered almost identical. At the same time, the averaging would reduce the mean phase noise term, $\widetilde{\psi}^{neigh}_{noise}$, which can be considered negligible compared with the deterministic terms. So, (8) can be simplified to,

$$\psi^{dif} \approx \psi^{dif}_{\triangle def} + \psi^{dif}_{\triangle \xi_{DEM}} + \psi^{central}_{noise} \quad (9)$$

where the first two terms are due to differences between the deformation and DEM error of the central pixels with respect to the neighboring ones. The averaging of the neighboring pixels produces phase terms that can be associated to a mean DEM error, $\widetilde{\xi}^{neigh}_{DEM}$, and to a mean deformation, $\widetilde{def}^{neigh}$, respectively. Regarding the deformation terms,

$$\psi^{dif}_{\triangle def} = \psi^{central}_{def} - \widetilde{\psi}^{neigh}_{def} \quad (10)$$

where its phase difference can be associated to a deformation difference, $\triangle def$, between central and mean neighboring pixels. Similarly, for the DEM error term,

$$\psi^{dif}_{\triangle \xi_{DEM}} = \psi^{central}_{\xi_{DEM}} - \widetilde{\psi}^{neigh}_{\xi_{DEM}} \quad (11)$$

where the phase can be associated to a DEM error difference, $\triangle \xi_{DEM}$.

The terms can be grouped in deterministic, $\psi^{dif}_{\triangle def}$ and $\psi^{dif}_{\triangle \xi_{DEM}}$, and random, $\psi^{central}_{noise}$.

c) Noise phase estimation: As (9) shows, the estimation of the noise phase of the central pixel, $\psi^{central}_{noise}$, would be affected by the two deterministic phase terms, $\psi^{dif}_{\triangle def}$ and $\psi^{dif}_{\triangle \xi_{DEM}}$. In practice and as a first approach, it can be assumed that both deformation and DEM error present also a spatial low-pass behaviour. As a consequence, the two deterministic terms of (9) can be neglected,

$$\psi^{dif}_{\triangle def} \approx 0 \text{ and } \psi^{dif}_{\triangle \xi_{DEM}} \approx 0. \quad (12)$$

Under this assumption $\psi^{dif} \approx \psi^{central}_{noise}$, or in other words, the differential phase is a good estimation of the central pixel noise.

d) TPC calculation: The estimated central pixel noise for each one of the M interferograms is used to determine the temporal phase coherence (TPC) of the dataset,

$$\hat{\gamma}_{TPC} = \frac{1}{M} \cdot \left| \sum_{i=1}^{M} e^{j \cdot \psi^{central}_{noise,i}} \right| \approx \frac{1}{M} \cdot \left| \sum_{i=1}^{M} e^{j \cdot \psi^{dif}_{i}} \right|. \quad (13)$$

Similarly to the classical interferometric coherence, values closer to 1 would indicate a good quality pixel while values closer to 0 a decorrelated one.

C. TPC for Different Interferogram Combinations

The interferogram dataset can be generated using two different approaches, as shown in Fig. 2. One is the single-master (SM) approach (Fig. 2(a)), in which all the interferograms share the same master image; the other is the multi-master (MM) approach (Fig. 2(b)), in which any free combination of images is allowed.

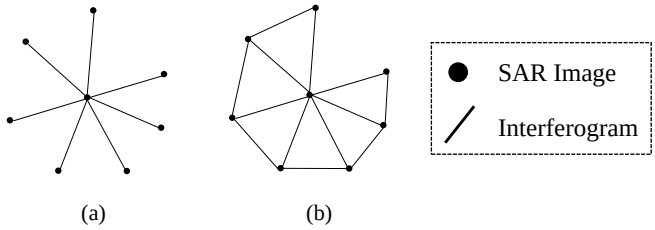

Fig. 2. Different types of interferogram combinations. (a) single-master (SM) interferogram combination; (b) multi-master (MM) interferogram combination.

The influence of the different interferograms' generating ways on the TPC has been studied by simulation. For each given phase standard deviation (phase STD) defined at SLC image level, 2000 realizations have been done. Different numbers of SAR images (ranging from 10 to 40) and different interferogram combinations (SM and MM cases) based on them have been generated. Then the corresponding measured $\hat{\gamma}^{SM}_{TPC}$ and $\hat{\gamma}^{MM}_{TPC}$ for SM and MM interferogram combinations are obtained by averaging all the 2000 realizations. The results are shown by Fig. 3.

From Fig. 3 we can find that the MM-TPC $\hat{\gamma}^{MM}_{TPC}$ is smaller than that of SM-TPC $\hat{\gamma}^{SM}_{TPC}$ for the same phase STD. Looking at the different cases presented in Fig. 3, the relationship between them is always located within the region defined by the lower bound $\hat{\gamma}^{MM}_{TPC} = (\hat{\gamma}^{SM}_{TPC})^2$, that would be obtained if all possible interferograms were used, and the upper bound $\hat{\gamma}^{MM}_{TPC} = \hat{\gamma}^{SM}_{TPC}$, the pure SM case.

Fig. 4 illustrates an example of relationship between $\hat{\gamma}^{SM}_{TPC}$ and $\hat{\gamma}^{MM}_{TPC}$ obtained from the real SAR data set presented in Section III. From the 31 SAR images, 30 SM and 79 MM interferograms have been generated. As expected, the relationship follows the bounds presented in Fig. 3. It has to be pointed out that the simulation considers the ideal case in which for any pixel its phase quality is identical in all images, while in the real data this condition is not fulfilled. It is reasonable to assume that there will be a certain distribution of phase qualities along the dataset. This difference justifies the distribution shown in Fig. 4.

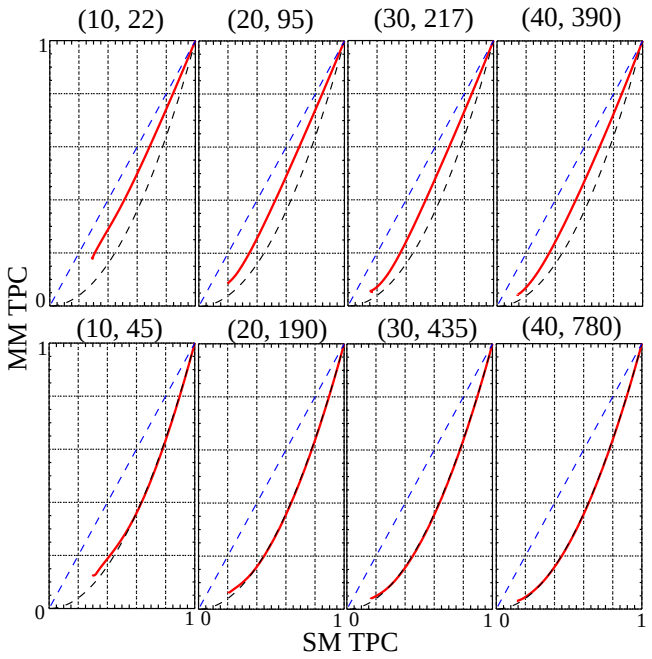

Fig. 3. Relationship between SM and MM interferograms' TPC (red line) for different cases. The blue and black dotted lines depict the upper ($\hat{\gamma}_{TPC}^{MM} = \hat{\gamma}_{TPC}^{SM}$) and lower bound ($\hat{\gamma}_{TPC}^{MM} = (\hat{\gamma}_{TPC}^{SM})^2$), respectively. The two numbers (m, n) on the top of each sub-figure represent the number of SAR images and generated interferograms, respectively.

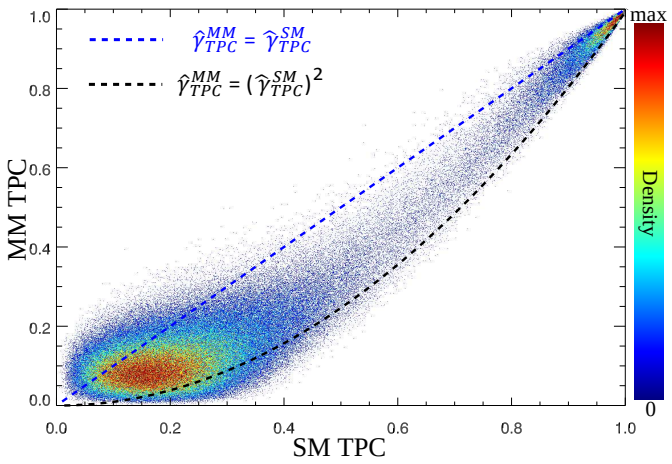

Fig. 4. Relationship between $\hat{\gamma}_{TPC}^{SM}$ and $\hat{\gamma}_{TPC}^{MM}$ for real SAR data.

D. Relation Between Estimated TPC and Phase Noise Standard Deviation

The goal is not estimating the TPC but the Phase Noise Standard Deviation (phase STD) of all pixels of the dataset. So it is necessary to determine the relationship between both. With it, an adequate threshold on TPC can be established to identify those pixels with a given phase quality.

Starting with the SM interferogram case the measured coherence, $\hat{\gamma}_{TPC}^{SM}$ can be related with with the phase standard deviation, $\sigma_{\psi_{SM}}$, with a simulation like in the previous section. For each phase STD, 2000 realizations have been simulated and then the corresponding mean coherence, $\hat{\gamma}_{TPC}^{SM}$, and standard deviation, $\sigma_{\hat{\gamma}_{TPC}^{SM}}$ have been obtained from all realizations. As expected, the results show a clear dependence on the number of images and its uncertainty decreases with the number of images. In the SM interferogram case each image of the dataset set, excepting the common master, appears only once in the generated interferograms and so, under the statistical point of view, the behaviour along the interferograms of each pixel can be considered as independent realizations.

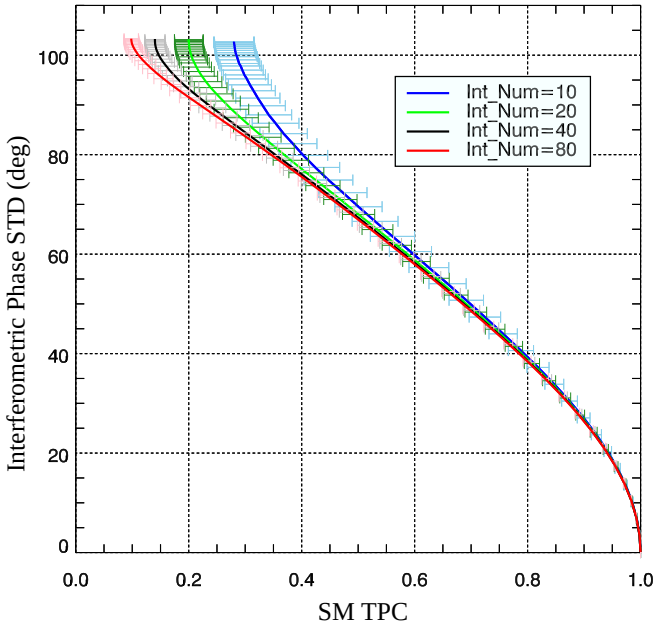

Fig. 5. Relationship between $\hat{\gamma}_{TPC}^{SM}$ and phase deviation $\sigma_{\psi_{SM}}$ for different SM interferogram groups obtained from simulation. The $\sigma_{\hat{\gamma}_{TPC}^{SM}}$ is also presented as error bars.

In the MM case most of the images will appear in more than one interferogram which means that with this approach the pixel's behavior will present some correlation along the interferogram dataset. To illustrate this phenomenon, the simulation between MM-TPC $\hat{\gamma}_{TPC}^{MM}$ and phase STD of four different interferogram data sets are presented in Fig. 6. It is worth to be noted that the first interferogram group is actually the SM interferogram case. Once again, the relationship depends, for a given number of images, on the number of interferograms generated.

E. Impact of $\triangle def$ and $\triangle \xi_{DEM}$ in TPC estimation

The assumption that both DEM error and deformation presents a low-pass behavior formulated in equation (12) can not be true. For instance, in urban areas strong variations of heights among buildings and streets can be expected. Similarly, deformation pattern can be different in a building with respect the surrounding ones or the street. If the assumption does not hold the two deterministic terms, $\psi_{\triangle def}^{dif}$ and $\psi_{\triangle \xi_{DEM}}^{dif}$, will behave as an additional sources of phase noise when evaluating the TPC. Both terms can be mathematically modeled with the classical DInSAR equations [7]. Regarding the term associated to the differences in the DEM error among the central and

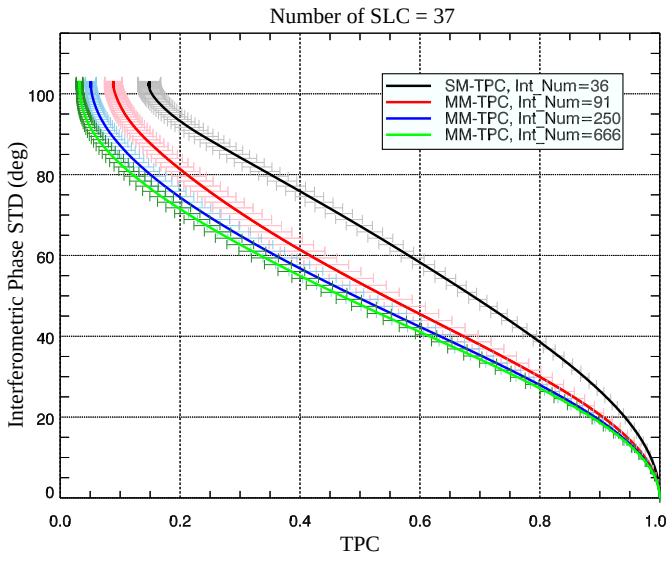

Fig. 6. Relationship between MM-TPC $\hat{\gamma}_{TPC}^{MM}$ and phase standard deviation for different MM interferogram groups obtained from simulation. The $\sigma_{\hat{\gamma}_{TPC}^{MM}}$ is also presented as error bars.

neighboring pixels, $\triangle\xi_{DEM} = \xi_{DEM}^{central} - \widetilde{\xi}_{DEM}^{neigh}$, the phase terms is,

$$\psi_{\triangle\xi_{DEM,i}}^{dif} = \frac{4\pi}{\lambda} \cdot \frac{B_{n,i}}{R_0 \cdot sin(\vartheta_0)} \cdot \triangle\xi_{DEM} \tag{14}$$

where $\lambda, B_{n,i}, R_0$ and ϑ_0 are the wavelength, the perpendicular baseline of the ith interferogram, the absolute range distance in the LOS direction between sensor and target, and the local incidence angle, respectively.

Similarly, the phase term due to deformation differences, $\triangle def_i = def_i^{central} - \widetilde{def}_i^{neigh}$, is,

$$\psi_{\triangle def_i}^{dif} = \frac{4\pi}{\lambda} \cdot \triangle def_i. \tag{15}$$

For both terms its phase standard deviation associated with its temporal behaviour can be mathematically modeled as a function of the standard deviation of spatial baselines, σ_{B_n} and the standard deviation of deformations, $\sigma_{\triangle def}$,

$$\sigma_{\psi_{\triangle\xi_{DEM}}^{dif}} = \frac{4\pi}{\lambda} \cdot \frac{\sigma_{B_n}}{R_0 \cdot sin(\vartheta_0)} \cdot \triangle\xi_{DEM} \tag{16}$$

and

$$\sigma_{\psi_{\triangle def}^{dif}} = \frac{4\pi}{\lambda} \cdot \sigma_{\triangle def}. \tag{17}$$

Equation (17) can be modified if it is assumed that deformation follows a lineal model, $def_i = v \cdot T_i$. With v the deformation velocity and T_i the temporal baseline of the ith interferogram. In such case equation (17) becomes,

$$\sigma_{\psi_{\triangle def}^{dif}} = \frac{4\pi}{\lambda} \cdot \triangle v \cdot \sigma_T \tag{18}$$

where $\triangle v = v^{central} - \widetilde{v}^{neigh}$ is the difference of deformation velocity of the central pixel and the neighboring ones, and σ_T the standard deviation of temporal baselines.

So, the overall standard deviation is,

$$\sigma_{\psi_{\xi_{\triangle\xi_{DEM}+\triangle def}}^{dif}} = \sqrt{(\sigma_{\psi_{\triangle\xi_{DEM}}^{dif}})^2 + (\sigma_{\psi_{\triangle def}^{dif}})^2} = \sqrt{(\frac{4\pi}{\lambda} \cdot \frac{\sigma_{B_n}}{R_0 \cdot sin(\vartheta_0)} \cdot \triangle\xi_{DEM})^2 + (\frac{4\pi}{\lambda} \cdot \sigma_{\triangle def})^2}. \tag{19}$$

If the linear model for deformation is assumed, $\sigma_{\triangle def_i}$ has to be replaced by $\triangle v \cdot \sigma_{T_i}$.

The impact of the combined errors has been simulated. It has to be pointed out that equation (19) represents the phase standard deviation for unwrapped phases. As phases are wrapped in practice, the original gaussian distribution for low noises tends to a uniform one as differences among central and neighboring pixels arise.

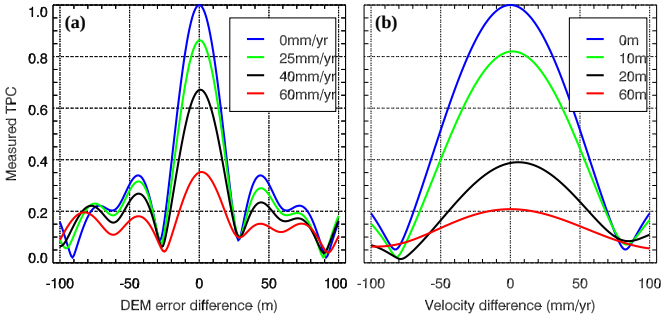

Fig. 7. (a) and (b) are the simulation results of the $\hat{\gamma}_{TPC}^{MM}$ for different combinations of $\triangle\xi_{DEM}$ and $\triangle v$. The number of images, interferograms and baselines distributions are identical to the Radarsat-2 dataset presented in the results section, as Fig. 8 shows.

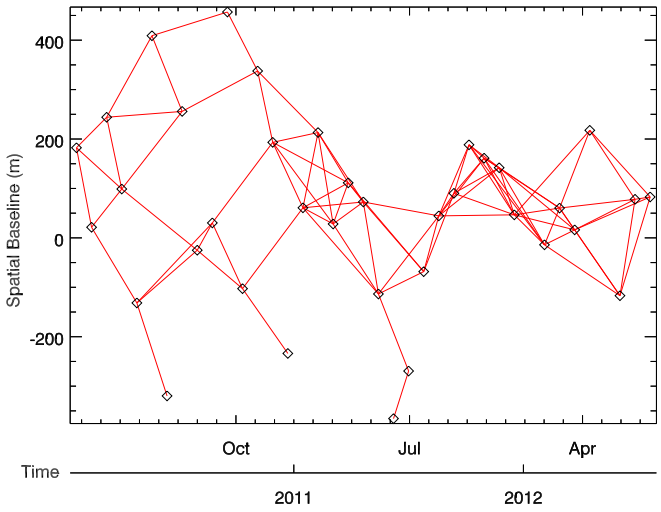

Fig. 8. Distribution of images for the Radarsat-2 dataset. The lines connecting image pairs indicate the interferogrmas generated.

Fig. 7 shows the $\hat{\gamma}_{TPC}^{MM}$ for different combinations of $\triangle\xi_{DEM}$ and $\triangle v$. The number of images, interferograms and temporal and spatial baselines are the same as the dataset of Radarsat-2 images that will be presented in Section III. The distribution of images and interferograms are shown in Fig. 8. In order to simply illustrate the impact of the errors on the TPC estimation the data has been considered noiseless. The

plots clearly show the degradation of the estimation of $\hat{\gamma}_{TPC}^{MM}$ as the two errors arise. Large errors would jeopardize the proper selection of pixels as good ones would be discarded.

F. Compensation of $\triangle v$ and $\triangle \xi_{DEM}$

For any pixel, $\triangle \xi_{DEM}$ can be assumed to be identical for all interferograms so it could be estimated. On the other side, $\triangle def$ can present a random behavior and it can not be estimated easily at this stage of the processing unless a linear model is assumed. In that case, $\triangle v$ can be also estimated.

Hooper use the Least Square (LS) method (as (20) shows) to estimate $\triangle \xi_{DEM}$ [18].

$$\triangle \xi_{DEM} = \frac{1}{N} \cdot \frac{\lambda}{4\pi} \cdot \sum_{i=1}^{N} \frac{R_0^i \cdot sin(\vartheta_0^i)}{B_{n,i}} \cdot \psi_i^{dif} \qquad (20)$$

where N is the number of interferograms. The estimation of $\triangle \xi_{DEM}$ may be unreliable if ψ_i^{dif} is wrapped, which can be expected when large baselines are combined with large DEM errors. Therefore, a more sophisticated algorithm, which utilizes a filter in frequency domain, has been proposed by Hooper to estimate $\psi_{noise}^{central}$ [19]. However, this method has a much higher computation burden. Other approaches, such as the least squares ambiguity decorrelation (LAMBDA) [21] method, can be used to estimate $\triangle \xi_{DEM}$, but it is computationally expensive as well.

In order to avoid the limitations of phase wrapping, the estimation of $\triangle \xi_{DEM}$ and $\triangle v$ can be done in the complex domain. The values of $\triangle \xi_{DEM}$ and $\triangle v$ can be estimated through the maximization of the cost function shown in (21),

$$\arg \max_{\substack{\triangle \xi_{DEM} \\ \triangle v}} \{\gamma_{TPC} = \frac{1}{M} \cdot | \sum_{i=1}^{M} e^{j \cdot (\psi_i^{dif} - \psi_{\triangle \xi_{DEM,i}}^{dif} - \psi_{\triangle def_i}^{dif})} |\} \qquad (21)$$

where $\psi_{\triangle \xi_{DEM,i}}^{dif}$ is the model defined in (14) and $\psi_{\triangle def_i}^{dif}$ the model defined in (18). This maximization in the complex plane has been successfully used in the implementation of CPT [7], [22] to estimate the DEM error and the linear velocity of deformation. Their accuracy depends on the distribution of the perpendicular and temporal baselines and the phase standard deviation (STD) of the interferograms $\sigma_{\psi_{noise}}$. With uniform baselines distributions, the correct values of $\triangle \xi_{DEM}$ and $\triangle v$ can be obtained even if a large amount of phases are wrapped.

Fig. 9(a) shows the $\hat{\gamma}_{TPC}^{MM}$ for different $\triangle v$ and $\triangle \xi_{DEM}$ as a function of $\sigma_{\psi_{noise}}$. The number of images, interferograms and baselines distribution is, once again, the same as the real dataset. The reference plot is for the errorless case, this is $\triangle v = 0$ and $\triangle \xi_{DEM} = 0$. As expected, $\hat{\gamma}_{TPC}^{MM}$ is degraded with the increasing errors and phase noise, $\sigma_{\psi_{noise}}$. If the errors are estimated and used to correct the interferogram's phase, the performance of $\hat{\gamma}_{TPC}^{MM}$ is improved and it behaves as the errorless case up to reasonable $\sigma_{\psi_{noise}}$ values. It has to be pointed out that the improvement of coherence is biased with noisy interfeograms as the model is adjusted to the noise and, as a consequence, the retrieved error differences are not realistic. So, for noise values over 50 deg the estimated differences are not reliable and the improvement in the measured TPC

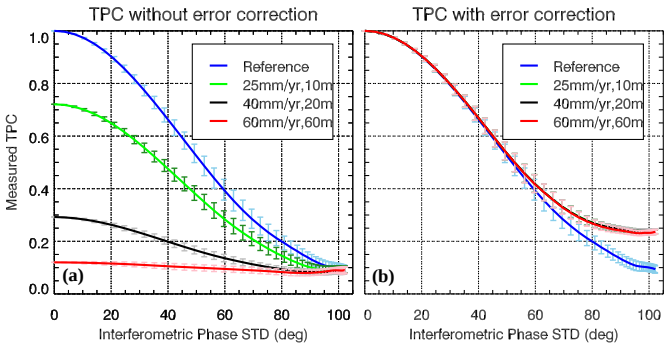

Fig. 9. (a) shows the $\hat{\gamma}_{TPC}^{MM}$ for different $\triangle v$ and $\triangle \xi_{DEM}$ as a function of $\sigma_{\psi_{noise}}$. The reference plot is for the errorless case. (b) shows the behavior of $\hat{\gamma}_{TPC}^{MM}$ after the errors have been estimated and corrected.

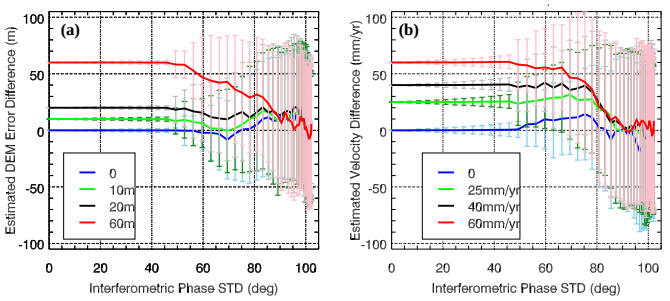

Fig. 10. Estimation of $\triangle \xi_{DEM}$ and $\triangle v$ for different $\sigma_{\psi_{noise}}$ levels. The vertical error bars indicate the result's standard deviation of uncertainty.

tends to an asymptotic value for all cases. Fig. 10 shows the retrieved differences and its corresponding error bars for the different phase noise levels simulated. The standard deviation of the results dramatically increases over the 50 deg of phase STD (or 0.5 of measured TPC), which can be established as the realistic limit of trustworthiness in the improvement. The good performance of the error estimation will be validated with real data in Section V.

III. Test Site and Data Set

Two test sites located in Barcelona city and Barcelona "El Prat" Airport have been chosen to evaluate the performance of TPC pixel selection strategy. As previous studies indicate, different subsidence phenomena occurred in the study area [23]–[25]. In this paper, 37 VV polarization Radarsat-2 SAR images, acquired from January 2010 to July 2012, are used to evaluate the effectiveness and feasibility of the proposed pixel selection algorithm. The SAR sensor works at C-band, with a revisit period of 24 days. The resolution of the SAR images is 5.1 and 4.7 m in azimuth and range directions, respectively.

IV. Results

The proposed TPC pixel selection algorithm has been integrated into UPC's DInSAR processing chain, i.e. the SUBSIDENCE-GUI, which is based on the Coherent Pixel Technique (CPT) [7], [22]. The ground deformation results presented in this paper have been obtained with this software.

The DInSAR processing consists mainly in three steps. Firstly, by setting the maximum temporal and spatial baseline as 200 m and 140 days, 91 small-baseline differential interferograms with an external DEM have been generated, as Fig. 8 shows. Then by using the two classical pixel selection methods, i.e. the amplitude dispersion (D_A), the spatial coherence (SPC) stability (using a moving averaging window to compute the coherence), and the new temporal phase coherence (TPC) algorithm, pixels with high phase quality have been identified. To make a fair comparison of the classical and the new approaches, the same phase standard deviation threshold (around 25°) is used for all cases during the pixel selection step. Finally, the CPT algorithm has been used to derive the deformation results over the study area.

The derived deformation maps for each selection method are shown in Fig. 11, where very similar subsidence trends are detected by all approaches. The derived subsidence patterns and deformation values are in good accordance with previous studies [23]–[25], which further validates the reliability of the results. The subsidence mainly occurred over the airport access road and Terminal T1 areas, and the maximum subsidence velocity reaches up to 2.5 cm/year. As the figure illustrates, the TPC approach has much better performance in pixels' density than the other two methods. Particularly, the TPC method is able to select 22,744 pixels, which accounts for about 318% and 146% of that obtained by D_A (7,150 pixels) and SPC (15,547 pixels) approaches. For the SPC case it has to be pointed out that as a moving averaging window has been used the pixels are not at full resolution. Due to the obvious improvement on pixels' density, TPC can detect at full resolution more detailed subsidence patterns than the other two methods.

V. Discussion

A. Compensation of $\triangle def$ and $\triangle \xi_{DEM}$ in TPC estimation with real data

In this section the impact of determining the DEM error difference ($\triangle \xi_{DEM}$) and deformation velocity difference ($\triangle def$), using equation (21), is studied with real data. From the Radarsat-2 data set an area in the city of Barcelona has been selected, where these errors are more likely to happen. The mean SAR amplitude and a Google Earth image of the area are shown by Fig. 12. As it can be seen from Fig. 12(b), the heights of buildings and streets varies a lot and so significant $\triangle \xi_{DEM}$ can be expected. On the other side, no significant deformations are expected [23]–[25].

The estimated TPC without (referred as TPC_{App}) and with (referred as TPC_{Opt}) $\triangle \xi_{DEM}$ and $\triangle def$ compensation are shown in Fig. 13(a) and (b), respectively. By comparing them, it can be found that the error compensation improves the estimated TPC values. This improvement can be more clearly observed in Fig. 13(c), where the difference between the two approaches is presented. Improvements are localized in areas with strong building elevation variations. Fig. 14 shows a scatter plot between TPC_{App} and TPC_{Opt}. Despite improvements are more significant for those pixels with lower TPC values (f.i., when TPC_{Opt} is smaller than 0.5) they are not reliable. As presented in Section II.F, for low TPC_{Opt} values the model has been adjusted to noise and the retrieved error differences present an extremely high uncertainty. A clear example of this wrong behavior is the improvement of TPC_{Opt} over the sea, which obviously is a fully decorrelated area. The only reliable improvement is for those pixels with TPC_{Opt} over 0.5.

The area highlighted by the rectangles in Fig. 13(a), (b) and (c) corresponds to the Agbar Tower and its vicinities. An optical Google Earth image of the area is shown in Fig. 13(d). The Agbar Tower, highlighted by a yellow circle in Fig. 13(d), is one of the landmark buildings of Barcelona and it has a height of around 144 m. Its remarkable height compared with the surrounding buildings and terrain can undermine the estimated of TPC if not compensated. After the error correction, TPC values of some pixels within this small area have been improved with values from around 0.1 (TPC_{App}) to 0.6 (TPC_{Opt}), which validates the effectiveness of $\triangle \xi_{DEM}$ compensation. Fig. 13(c) clearly shows the improvement on TPC estimation in the area.

If 0.7 is set as the TPC threshold for pixel selection in this area, the number of pixels selected by TPC_{App} and TPC_{Opt} are 18329 (11.4%) and 18817 (11.7%), respectively. The improvement on pixel density by using TPC_{Opt} is not significant (only 0.3%) w.r.t. that of TPC_{App}. This indicates that TPC_{App} can be a good metric for pixel selection even in urban areas where heights may vary a lot. In this way, by sacrificing a very small amount of selected pixels, the TPC estimation processing time can be dramatically reduced.

B. Influence of the Neighboring Window Size on TPC Estimation

The mean phase of the neighboring pixels, $\widetilde{\psi}^{neigh}$ in equation (7), is determined with an estimation window of a given size. In order to evaluate the impact of its size in the estimation of the central pixel TPC, the TPC of the airport test site has been estimated with three different window sizes of 21×21, 31×31 and 41×41. An improved version of TPC has been defined with an adaptive neighboring window size by simply taking the maximum TPC among the values obtained from the three window sizes.

The scatter plot of the TPC values for all pixels of the dataset for neighboring window sizes of 21×21 and 41×41 is depicted in Fig. 15(a). For values above 0.5 the TPC values estimated in both cases are very similar while for lower values differences start to arise. The same conclusion can be applied if the 41×41 case is replaced by the adaptive window, as shown in Fig. 15(b). The improvement of estimated TPCs with the adaptive window is once again not really noticeable for high quality pixels. Smaller neighboring window sizes may lead to unreliable TPC estimations, while spatial high-pass components (relative to $\psi^{central}$) could be brought into $\widetilde{\psi}^{neigh}$ by bigger ones. As we are interested in high quality pixels, it is enough to use window sizes not bigger than 21×21 in our case, as larger or the adaptive one increases the computational burden with not real improvement on the final results.

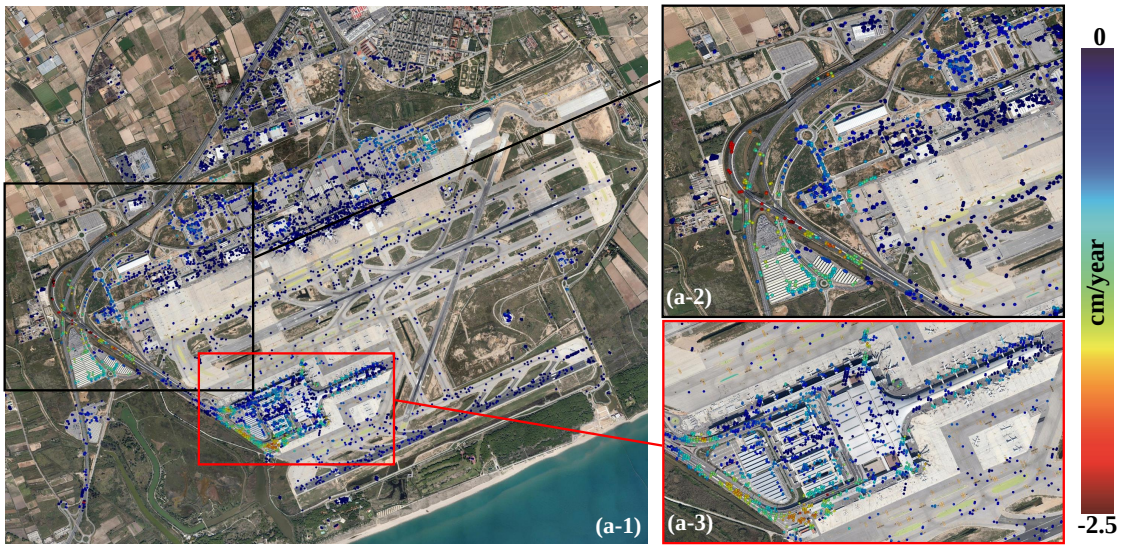

(a) DA (7150)

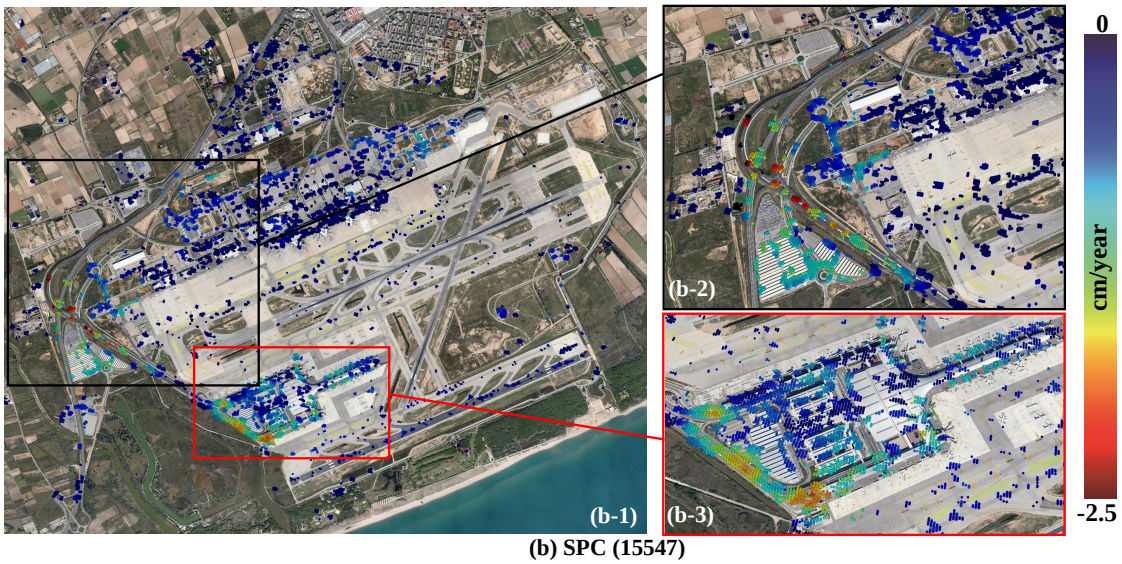

(b) SPC (15547)

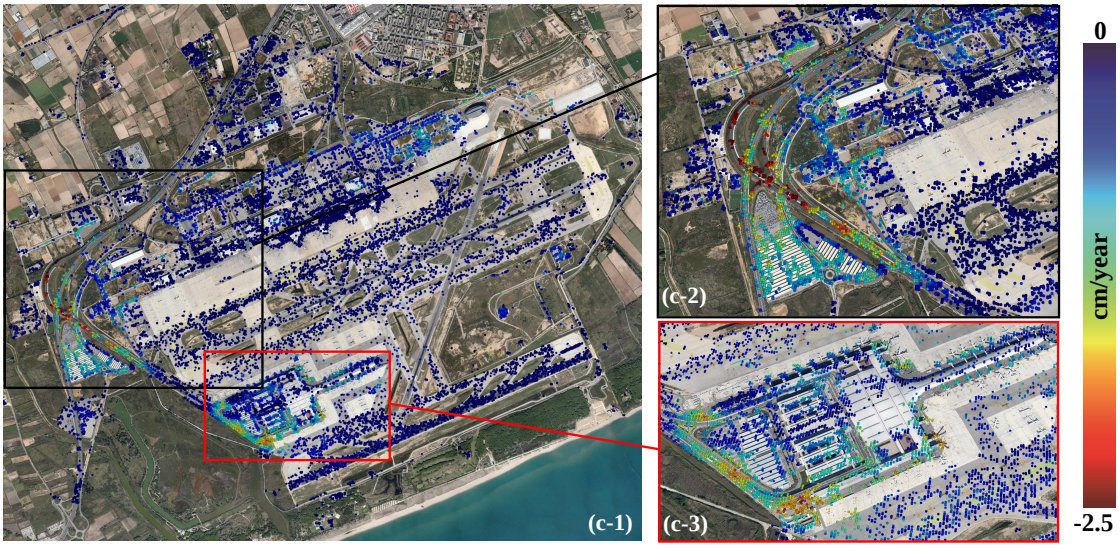

(c) TPC (22744)

Fig. 11. Deformation velocity map in Barcelona "El Prat" Airport retrieved by (a) the PS (D_A) approach, (b) the classical spatial coherence (SPC) approach, and (c) the proposed temporal phase coherence (TPC) approach. The number in the bracket represents the amount of selected pixels by each approach.

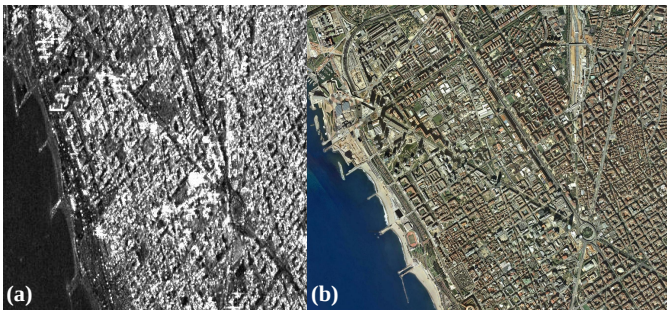

Fig. 12. (a) Mean SAR amplitude image and (b) Google Earth image of the Barcelona urban area.

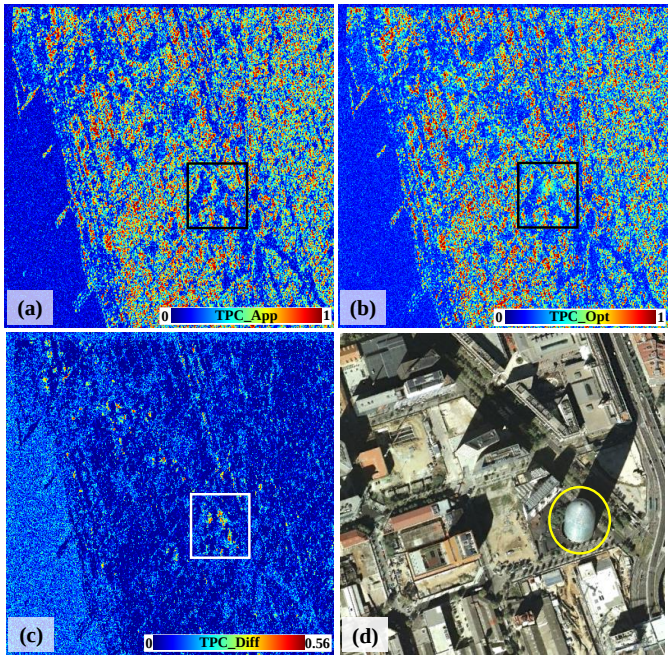

Fig. 13. (a) TPC without error compensation (i.e. TPC_{App}), (b) TPC with error compensation (i.e. TPC_{Opt}) of the Barcelona urban area. (c) Difference between TPC_{Opt} and TPC_{App}, (d) the famous Agbar Tower (highlighted by the yellow circle) and its vicinities.

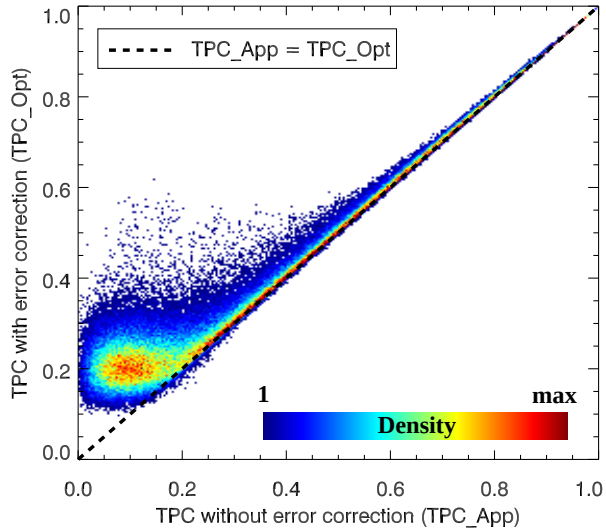

Fig. 14. Scatter plot between TPC_{App} (Fig. 13(a)) and TPC_{Opt} (Fig. 13(b)).

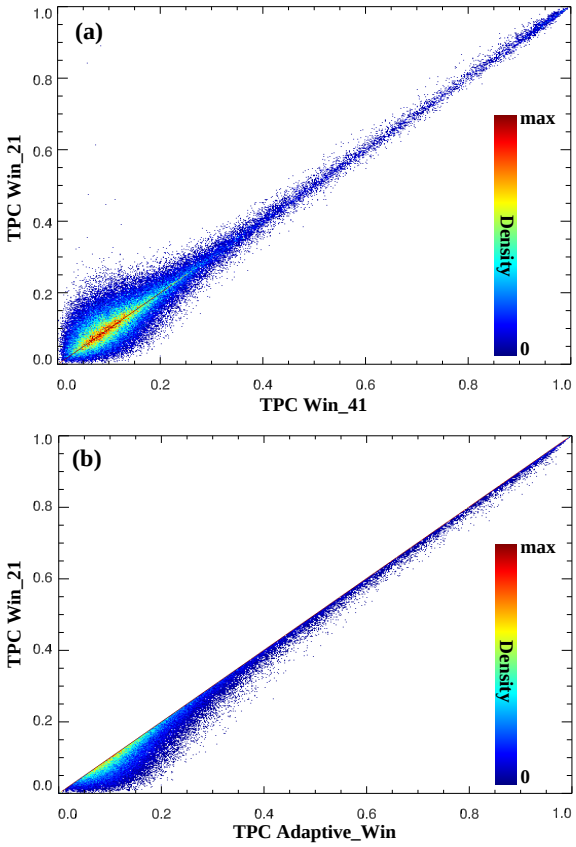

Fig. 15. The influence of different neighboring window sizes on TPC estimation. (a) Scatter plot between TPC estimated with 41 $\times$ 41 and 21 $\times$ 21 neighboring window sizes; (b) scatter plot between TPC estimated by the adaptive and 21 $\times$ 21 neighboring window sizes.

C. TPC Versus D_A

In order to compare the performance of TPC with D_A in pixel selection, Fig. 16(a) shows a scatter plot of all pixels of the dataset over Barcelona airport test site. Those pixels with a TPC less than 0.3 mainly corresponded to D_A greater than 0.4, and as expected D_A values decrease as the ones of TPC increase. Since small D_A and big TPC indicate high phase quality, the effectiveness of TPC as a phase quality estimator is thus validated. As Fig. 16(b) demonstrates, almost all pixels with D_A smaller than 0.3 present a TPC greater than 0.7, the selection threshold used in the paper. Many pixels with higher D_A, from 0.3 to 0.55 are also selected by TPC, which dramatically helps to increase the pixels' density. Most of them can be associated with the so-called DS pixels, for instance the large number detected over the runways of the airport as shown in Fig. 11(c). To conclude, TPC is a reliable and effective estimator of phase quality at full resolution. Comparing with D_A, on the one hand, it is able to detect high quality pixels from both PSs and DSs that contributes to obtain much better pixel densities. On the other, it does not require a minimum number of SAR images as strict as D_A needs, although the larger the number the better the estimation will be.

D. TPC Versus SPC

A similar analysis has been made comparing TPC and SPC performances, despite the resolution is not the same in the two approaches. SPC has used a moving averaging window of 5 $\times$ 3 (azimuht $\times$ range) to preserve the number of pixels of the original SLC. Fig. 16(c) shows the scatter plot of TPC versus SPC. An important difference if compared with D_A, and mostly caused by the inherent multilooking of SPC, is that many pixels with small TPC have been selected by the SPC approach, as Fig. 16(d) shows. These pixels are mainly those presenting low phase qualities but with high quality ones on its neighbourhood. If the high quality ones also present higher amplitudes, the multilooking with a moving averaging window makes the bad ones "better" than they really are. This phenomena can be observed in Fig. 11(b), where some SPC selected pixels are distributed as small clusters centred in the location of high quality ones selected with TPC.

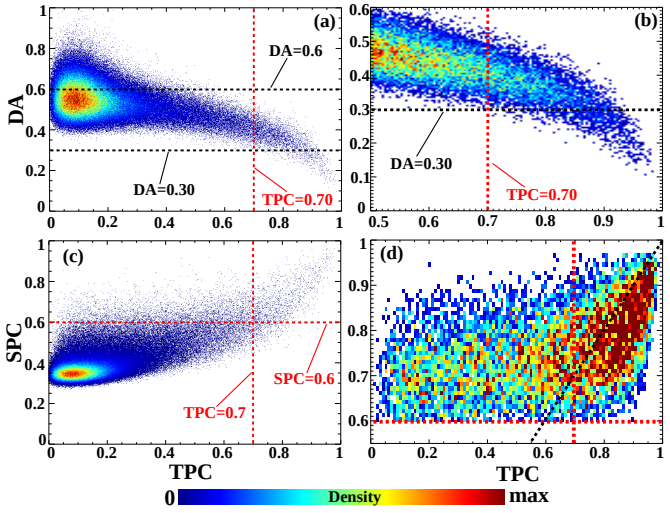

Fig. 16. Scatter plots between different phase quality estimators. (a) Scatter plot of TPC vs D_A, and (b) is the close-up of (a) when D_A is less than 0.6 and TPC is above 0.5; (c) scatter plot of TPC vs SPC, and (d) is the close-up of (c) when SPC is bigger than 0.6.

E. Deformation Estimation with a Reduced Number of SAR Images with the TPC Approach

To study the TPC approach's effectiveness with reduced numbers of SAR images, 14 SAR images (less than $1/3$ of the original ones) of the Barcelona airport data set have been selected for the test. With these SAR images a total of 47 small-baseline differential interferograms have been generated, as Fig. 17 shows.

The TPC related with the 14 images (i.e. TPC_{14}) has been estimated and pixels have been selected with the same threshold as with the previous processing. Fig. 18 shows the linear deformation results retrieved. A total of 22,891 pixels have been obtained, which is roughly the same amount obtained with the 37 SAR images, 22,744 pixels shown in Fig. 11(c). There are some differences between the deformation results obtained by the TPC approach with 14 and 37 SAR images, which can be justified by the fact that SAR images

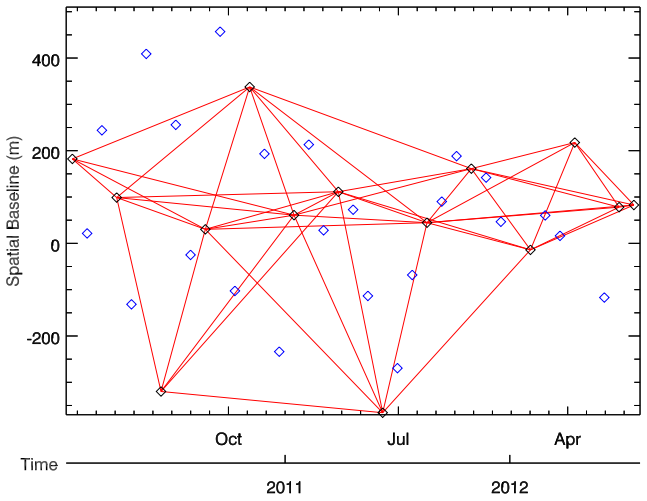

Fig. 17. Distribution of the 14 selected Radarsat-2 SAR images (black diamonds). The blue diamonds represent SAR images not being selected. The red lines connecting image pairs indicate the 47 generated interferogrmas.

acquiring at different dates are employed. Nevertheless, the location and extension of the different deformation bowls are very similar in both cases. This test validates the capability of TPC approach to work with reduced sets of SAR images.

VI. Comparison with other PSI Algorithms

The detailed comparison between the TPC approach and the two classical pixel selection strategies algorithms, i.e. the PS and SBAS techniques, have been made in the previous sections. To conclude, comparing with the PS method (based on D_A), more pixels can be selected by the TPC approach, and it is also able to work with a reduced number of SAR images. Comparing with SBAS (based on SPC), on the one hand, TPC approach selects pixels at full resolution. On the other hand, TPC approach does not improve pixels' interferometric phase quality, while the SBAS method does as the averaging improves phase quality but reduces the resolution.

The time costs for D_A, SPC and TPC calculations (not including the deformation estimation just the pixel selection step) over Barcelona airport area are 10.4 seconds, 48.5 seconds and 38.5 seconds, respectively. This indicates TPC can be efficiently calculated as D_A and SPC, making it a computational affordable phase quality metric for pixel selection in most cases. This test has been carried out on a workstation equipped with an 8-core Intel(R) Xeon(R) E5620 processor (2.4 GHz) and 60 GB of RAM. The implementation is in IDL. Compared with the overall processing time, pixel selection step is not a bottleneck for the overall processing time.

Comparing with advanced PSI techniques, like the phase linking [11], SqueeSAR [12] and other sophisticated algorithms [14], [15], [17] which are based on adaptive filtering or phase optimization methods, the advantage of the TPC approach is its simplicity and much lower computational burden. However, in areas where noisy interferometric phases needed to be optimized before pixel selection and deformation

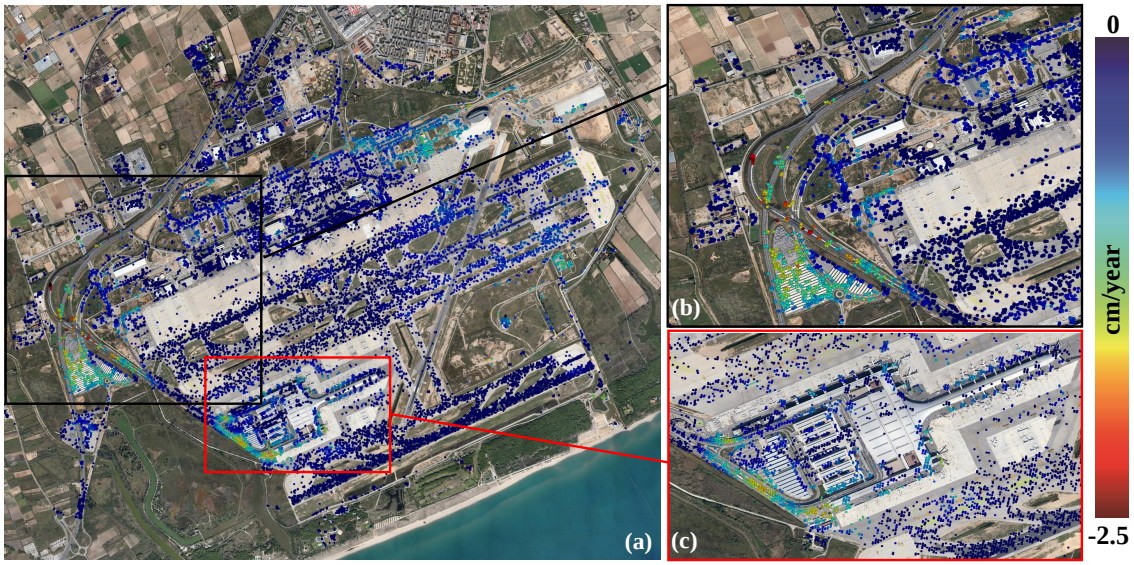

Fig. 18. Deformation velocity map in Barcelona airport derived by the TPC approach with 14 SAR images.

estimation, the advanced PSI algorithms would obviously perform better.

VII. Conclusion

In this paper, a full-resolution InSAR phase quality estimator, i.e. the temporal phase coherence (TPC), has been proposed and used to identify high quality pixels in SAR images. Instead of using the temporal variation of pixels' amplitude like D_A or the temporal stability of the coherence, TPC estimates pixels' phase quality directly from its interferometric phase noise at full resolution. For each pixel, the interferometric phase systematic terms are firstly eliminated in order to leave just the noise term in the interferometric phase. Then, the TPC is calculated based on the pixel-based noise phase term of all interferograms.

The impact of the interferograms' generation way (single-master (SM) or the multi-master (MM)) on TPC estimation has been studied. It is found that the relationship between SM-TPC $\hat{\gamma}_{TPC}^{SM}$ and MM-TPC $\hat{\gamma}_{TPC}^{MM}$ is constrained by the lower bound $\hat{\gamma}_{TPC}^{MM} = (\hat{\gamma}_{TPC}^{SM})^2$ and the upper bound $\hat{\gamma}_{TPC}^{MM} = \hat{\gamma}_{TPC}^{SM}$. To better complete the pixel selection, the relationship between TPC and phase standard deviation (STD) has been derived through simulation. Thus, the TPC threshold can be accurately determined according to the requirement of the phase STD of the pixels. The influence of the neighboring window size on the value of TPC has been studied, as well. For the Barcelona airport data set, it is found that window sizes larger than 21 $\times$ 21 do not imply any noticeable improvement in the results and increase the processing time. Considering efficiency and reliability, window sizes of 21 $\times$ 21 are a good choice for TPC estimation.

To validate the feasibility of the proposed pixel selection algorithm, it has been tested together with the other two classical approaches (D_A and SPC). The detected deformation patterns of all three methods over Barcelona Airport are very similar and consistent with previous studies, which validates the feasibility and effectiveness of TPC. Comparing the results obtained with the three methods, TPC shows some advantages. When comparing with D_A, besides the pixels selected by D_A it can identify much more other (about 3.2 times of that obtained by the D_A approach over the Barcelona airport study area) as it is able to detect stable pixels, independently if they are PSs or DSs. Moreover, it is more flexible regarding the number of SAR images necessary for a reliable selection. When comparing with SPC, TPC preserves the original resolution of the SAR image as no multilooking is applied. Low quality pixels surrounded by high quality ones will not be wrongly selected as the multilooking causes an overestimation of its quality. Similarly, isolated high quality pixels have a lower probability to be underestimated due to their low quality neighbors. As a result, more pixels can be selected (about 1.5 times of that obtained by SPC approach over the study area).

The computation cost of TPC, which is determined mainly by the size of the neighboring window, is low and affordable for all cases. This pixel selection strategy is also easy to implement and incorporate into any advanced PSI processor.

Finally, the method has also been applied to high-resolution X-band SAR data [26]. The dataset of 32 staring spotlight mode TerraSAR-X images over a landslide in Canillo (Andorra) have proved the good performance of TPC for detecting stable pixels from both PSs and DSs at this band. Narrow roads surrounded by vegetated areas with low reflectivity, clear example of DSs, have been selected as they present a very stable phase along time.

Acknowledgment

The authors would like to thank Dr. Ruben Iglesias and the reviewers for their constructive ideas and suggestions. The authors would also like to thank the Institut Cartografic i Geologic de Catalunya (ICGC) for providing the DEM used in the generation of the differential interferograms. The Radarsat-2 images were provided by MDA in the framework of the

scientific project SOAR-EU 6779. Optical images provided by GoogleEarth.

REFERENCES

[1] A. K. Gabriel, R. M. Goldstein, and H. A. Zebker, "Mapping small elevation changes over large areas: differential radar interferometry," *Journal of geophysical research: solid earth*, vol. 94, no. B7, pp. 9183–9191, 1989.

[2] R. Bamler and P. Hartl, "Synthetic aperture radar interferometry," *Inverse problems*, vol. 14, no. 4, p. R1, 1998.

[3] R. Bürgmann, P. A. Rosen, and E. J. Fielding, "Synthetic aperture radar interferometry to measure Earths surface topography and its deformation," *Annual review of earth and planetary sciences*, vol. 28, no. 1, pp. 169–209, 2000.

[4] H. A. Zebker and J. Villasenor, "Decorrelation in interferometric radar echoes," *IEEE Transactions on geoscience and remote sensing*, vol. 30, no. 5, pp. 950–959, 1992.

[5] A. Ferretti, C. Prati, and F. Rocca, "Permanent scatterers in SAR interferometry," *IEEE Transactions on geoscience and remote sensing*, vol. 39, no. 1, pp. 8–20, 2001.

[6] P. Berardino, G. Fornaro, R. Lanari, and E. Sansosti, "A new algorithm for surface deformation monitoring based on small baseline differential SAR interferograms," *IEEE Transactions on Geoscience and Remote Sensing*, vol. 40, no. 11, pp. 2375–2383, 2002.

[7] O. Mora, J. J. Mallorqui, and A. Broquetas, "Linear and nonlinear terrain deformation maps from a reduced set of interferometric SAR images," *IEEE Transactions on Geoscience and Remote Sensing*, vol. 41, no. 10, pp. 2243–2253, 2003.

[8] R. Lanari, O. Mora, M. Manunta, J. J. Mallorquí, P. Berardino, and E. Sansosti, "A small-baseline approach for investigating deformations on full-resolution differential SAR interferograms," *IEEE Transactions on Geoscience and Remote Sensing*, vol. 42, no. 7, pp. 1377–1386, 2004.

[9] J.-S. Lee, K. W. Hoppel, S. A. Mango, and A. R. Miller, "Intensity and phase statistics of multilook polarimetric and interferometric SAR imagery," *IEEE Transactions on Geoscience and Remote Sensing*, vol. 32, no. 5, pp. 1017–1028, 1994.

[10] R. Touzi and A. Lopes, "Statistics of the stokes parameters and of the complex coherence parameters in one-look and multilook speckle fields," *IEEE Transactions on Geoscience and Remote Sensing*, vol. 34, no. 2, pp. 519–531, 1996.

[11] A. M. Guarnieri and S. Tebaldini, "On the exploitation of target statistics for SAR interferometry applications," *IEEE Transactions on Geoscience and Remote Sensing*, vol. 46, no. 11, pp. 3436–3443, 2008.

[12] A. Ferretti, A. Fumagalli, F. Novali, C. Prati, F. Rocca, and A. Rucci, "A new algorithm for processing interferometric data-stacks: SqueeSAR," *IEEE Transactions on Geoscience and Remote Sensing*, vol. 49, no. 9, pp. 3460–3470, 2011.

[13] P. Guccione, A. Monti-Guarnieri, and S. Tebaldini, "Stable target detection and coherence estimation in interferometric SAR stacks," *IEEE Transactions on Geoscience and Remote Sensing*, vol. 50, no. 8, pp. 3171–3178, 2012.

[14] Y. Wang, X. X. Zhu, and R. Bamler, "Retrieval of phase history parameters from distributed scatterers in urban areas using very high resolution SAR data," *ISPRS Journal of Photogrammetry and Remote Sensing*, vol. 73, pp. pp–89, 2012.

[15] G. Fornaro, S. Verde, D. Reale, and A. Pauciullo, "CAESAR: An approach based on covariance matrix decomposition to improve multibaseline–multitemporal interferometric SAR processing," *IEEE Transactions on Geoscience and Remote Sensing*, vol. 53, no. 4, pp. 2050–2065, 2015.

[16] C.-A. Deledalle, L. Denis, F. Tupin, A. Reigber, and M. Jäger, "NL-SAR: A unified nonlocal framework for resolution-preserving (Pol)(In) SAR denoising," *IEEE Transactions on Geoscience and Remote Sensing*, vol. 53, no. 4, pp. 2021–2038, 2015.

[17] N. Cao, H. Lee, and H. C. Jung, "A phase-decomposition-based PSInSAR processing method," *IEEE Transactions on Geoscience and Remote Sensing*, vol. 54, no. 2, pp. 1074–1090, 2016.

[18] A. Hooper, H. Zebker, P. Segall, and B. Kampes, "A new method for measuring deformation on volcanoes and other natural terrains using InSAR persistent scatterers," *Geophysical research letters*, vol. 31, no. 23, 2004.

[19] A. Hooper, P. Segall, and H. Zebker, "Persistent scatterer interferometric synthetic aperture radar for crustal deformation analysis, with application to volcán alcedo, galápagos," *Journal of Geophysical Research: Solid Earth*, vol. 112, no. B7, 2007.

[20] R. F. Hanssen, *Radar interferometry: data interpretation and error analysis*. Springer Science & Business Media, 2001, vol. 2.

[21] P. J. Teunissen, "The least-squares ambiguity decorrelation adjustment: a method for fast GPS integer ambiguity estimation," *Journal of geodesy*, vol. 70, no. 1, pp. 65–82, 1995.

[22] P. Blanco-Sanchez, J. J. Mallorquí, S. Duque, and D. Monells, "The coherent pixels technique (CPT): An advanced DInSAR technique for nonlinear deformation monitoring," *Pure and Applied Geophysics*, vol. 165, no. 6, pp. 1167–1193, 2008.

[23] R. Iglesias, D. Monells, X. Fabregas, J. J. Mallorqui, A. Aguasca, and C. Lopez-Martinez, "Phase quality optimization in polarimetric differential SAR interferometry," *IEEE transactions on geoscience and remote sensing*, vol. 52, no. 5, pp. 2875–2888, 2014.

[24] V. D. Navarro-Sanchez, J. M. Lopez-Sanchez, and L. Ferro-Famil, "Polarimetric approaches for persistent scatterers interferometry," *IEEE Transactions on Geoscience and Remote Sensing*, vol. 52, no. 3, pp. 1667–1676, 2014.

[25] V. D. Navarro-Sanchez and J. M. Lopez-Sanchez, "Spatial adaptive speckle filtering driven by temporal polarimetric statistics and its application to PSI," *IEEE Transactions on Geoscience and Remote Sensing*, vol. 52, no. 8, pp. 4548–4557, 2014.

[26] F. Zhao, J. Mallorqui, R. Iglesias, J. Gili, and J. Corominas, "Landslide monitoring using multi-temporal SAR interferometry with advanced persistent scatterers identification methods and super high-spatial resolution TerraSAR-X images," *Remote Sensing*, vol. 10, no. 6, p. 921, 2018.

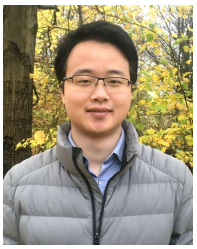

Feng Zhao (S'17) received the M.S. degrees in geodesy and surveying engineering from China University of Mining and Technology, Xuzhou, China, in 2016. He is currently working toward the Ph.D. degree at the Universitat Politècnica de Catalunya, Barcelona, Spain.

He joined the CommSensLab, Universitat Politècnica de Catalunya, in September 2016, where his main work focuses on the development of advanced pixel selection and optimization algorithms for multi-temporal (Pol)DInSAR techniques. His research interests include advanced multi-temporal InSAR techniques and its application on terrain deformation detection.

Jordi J. Mallorqui (S'93-M'96-SM'13) was born in Tarragona, Spain, in 1966. He received the Ingeniero and Doctor Ingeniero degrees in telecommunications engineering from the Universitat Politècnica de Catalunya (UPC), Barcelona, Spain, in 1990 and 1995, respectively.

Since 1993, he has been teaching with the School of Telecommunications Engineering of Barcelona, UPC, first as an Assistant Professor, later in 1997 as an Associate Professor, and since 2011 as a Full Professor. His teaching activity involves microwaves, radionavigation systems, and remote sensing. He spent a sabbatical year with the Jet Propulsion Laboratory, Pasadena, CA, USA, in 1999, working on interferometric airborne synthetic aperture radar (SAR) calibration algorithms. He is currently working on the application of SAR interferometry to terrain-deformation monitoring with orbital, airborne, and ground data; vessel detection and classification from SAR images; and 3-D electromagnetic (EM) simulation of SAR systems. He has published more than 100 papers on microwave tomography, EM numerical simulation, and SAR processing, interferometry, and differential interferometry in refereed journals and international symposia.